Structural origin of room-temperature ferroelectricity in spark-plasma sintered $DyCrO_3$ and $LaCrO_3$

Suryakanta Mishra,[1] Keerthana ,[2] Krishna Rudrapal,[3] Biswajit Jana,[4] Kazi Parvez Islam,[1] Archna Sagdeo,[5,6] Ayan Roy Chaudhuri,[3,4] Venimadhav Adyam,[2] and Debraj Choudhury[1,*]

[1]*Department of Physics, Indian Institute of Technology Kharagpur, Kharagpur 721302, India*
[2]*Cryogenic Engineering Centre, Indian Institute of Technology Kharagpur, Kharagpur 721302, India*
[3]*Advanced Technology Development Centre, Indian Institute of Technology Kharagpur, Kharagpur 721302, India*
[4]*Materials Science Centre, Indian Institute of Technology Kharagpur, Kharagpur 721302, India*
[5]*Accelerator Physics and Synchrotrons Utilization Division, Raja Ramanna Center for Advanced Technology, Indore 452013, India*
[6]*Homi Bhabha National Institute, Training School Complex, Anushakti Nagar, Mumbai 400094, India*

(Received 14 February 2023; accepted 8 June 2023; published 20 June 2023)

Identification of novel multiferroic materials with high-ordering temperatures remains at the forefront of condensed matter physics research. Recently, room-temperature ferroelectricity of structural origin, arising from off-centering displacements of Gd and Cr ions, has been identified in spark-plasma sintered (SPS) $GdCrO_3$ [Suryakanta Mishra *et al.*, Phys. Rev. B **104**, L180101 (2021)]. Here, using a similar synthesis protocol (involving SPS), we have been able to engineer room-temperature ferroelectricity (FE) from a similar mechanism in two otherwise nonferroelectric $RCrO_3$ (R= rare-earth) compounds, namely, $DyCrO_3$ (which is reported as a quantum paraelectric) and $LaCrO_3$ (which is already known to be paraelectric). Room-temperature FE in SPS-$LaCrO_3$ and SPS-$DyCrO_3$ is confirmed through various electrical, calorimetric, and synchrotron-based structural investigations. Out of these two emergent room-temperature FE materials, SPS-$LaCrO_3$ also undergoes a high-temperature antiferromagnetic ordering at 290 K, thus coming very close to becoming the first room-temperature multiferroic material in this promising family of $RCrO_3$ compounds.

DOI: 10.1103/PhysRevB.107.214104

I. INTRODUCTION

Multiferroic materials, i.e., those that are simultaneously ferroelectric (FE) and exhibit spontaneous magnetic ordering (such as ferromagnetism/antiferromagnetism), are extremely promising for both fundamental as well as applied condensed matter physics research [1–7]. For multiferroic materials to exhibit large magnetoelectric coupling, it becomes desirable that FE and spontaneous magnetic ordering emerge from the same structural unit; however, they are usually contraindicated in most materials. For example, the "d^0-ness", i.e., $3d^0$ (and hence diamagnetic) character of the transition-metal B cation in ABO_3 perovskite-related compounds, has often been stressed to be necessary to give rise to FE arising from cooperative off-center displacement of the B cations away from the negative charge center within the corresponding BO_6 octahedral cages. For example, in $BaTiO_3$, FE arises due to cooperative off-centering of $Ti^{4+}(3d^0)$ ions within the corresponding TiO_6 octahedra [8–10]. In the case of ABO_3 compounds containing a non-d^0 B cation, competing nonpolar lattice instabilities related to antiferrodistortive (AFD) rotation modes of the BO_6 octahedra become energetically more favorable and thus compete with the polar off-centering mode [schematic visualizations of the AFD and FE instability modes are shown in Figs. 1(a) and 1(b)] [11–18]. Following theoretical predictions [11,19,20], it has now been verified experimentally that through appropriate lattice strain, it becomes possible to tilt the energy balance away from the nonpolar AFD modes and favor the polar off-centering mode in some ferroelectric $AMnO_3$ (A = Sr, Ba, Ca) compounds containing the non-d^0 $Mn^{4+}(3d^3)$ ion [21–23]. Large Born-effective charges and off-centering were detected for the Mn^{4+} ion in these $AMnO_3$ compounds, suggesting their dominant contribution to the observed FE [11,19].

The competition between AFD and FE instability modes is also very common in orthorhombic $RCrO_3$ [24,25], which constitute an emerging class of multiferroic compounds. For example, FE is observed to arise concomitant with the antiferromagnetic (AFM) ordering at ≈170 K in standard solid-state sintered (SS) $GdCrO_3$ [26]. The similar ordering temperature for FE and AFM in most $RCrO_3$ (although much below room temperature) has led to contrasting reports in regards to the origin of FE, i.e., whether of structural or magnetic origin [26]. Recently, by applying uniaxial pressure at high temperatures through spark-plasma sintering (SPS), we have stabilized FE at room temperature in SPS $GdCrO_3$, which still undergoes AFM ordering below ≈170 K [27]. FE in SPS $GdCrO_3$, thus, clearly has a structural origin in the noncentrosymmetric $Pna2_1$ space group (also responsible for FE in SS $GdCrO_3$ below ≈170 K) that involves polar, though opposite, off-center displacements for Cr and Gd ions [25,27]. Some members of the $RCrO_3$ family are, however, nonferroelectrics, such as $DyCrO_3$, which is a quantum paraelectric

*debraj@phy.iitkgp.ac.in

 ©2023 American Physical Society

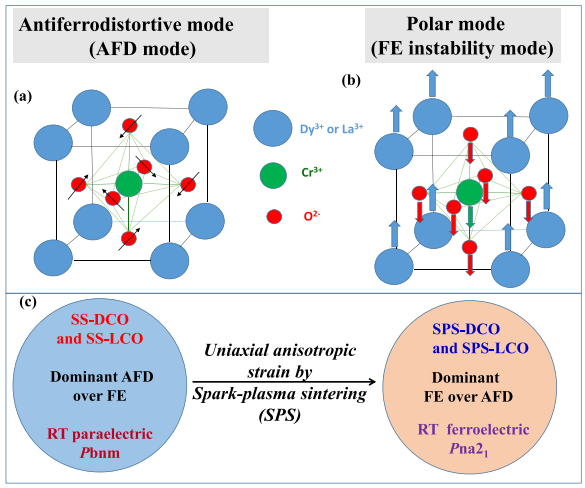

FIG. 1. Schematic visualization of (a) antiferrodistortive mode (AFD) and (b) polar mode (FE instability mode). (c) With the application of uniaxial anisotropic strain on SS-DCO and SS-LCO during spark-plasma sintering (SPS), the FE mode seems to get stabilized compared to the AFD mode, resulting in room-temperature ferroelectricity arising from the noncentrosymmetric $Pna2_1$ phase in SPS-DCO and SPS-LCO. DCO: $DyCrO_3$; LCO: $LaCrO_3$; SS: solid-state synthesized.

[28] (quantum fluctuations and AFD instabilities suppress FE order at low temperatures [29]), and $LaCrO_3$, which is a paraelectric [30–32]. Interestingly, although first-principles calculations deduce large Born-effective charges for La and Cr ions in $LaCrO_3$ (similar to $GdCrO_3$ and some other $RCrO_3$ compounds) that suggest an incipient FE instability [18,25,33,34], the FE state has never been experimentally realized in $DyCrO_3$ or in $LaCrO_3$ at any temperatures.

Here, we show that by adopting a dual-synthesis protocol involving SPS, room-temperature FE can be engineered in $DyCrO_3$ (also in $LaCrO_3$) much above the corresponding AFM ordering temperature. Room-temperature intrinsic FE is verified using positive up–negative down (PUND) and piezoresponse force microscopy (PFM) measurements. The net FE distortion at room temperature due to stabilization of the noncentrosymmetric $Pna2_1$ phase involves dominant off-center displacements of R^{3+} ions in opposite direction to the Cr^{3+} off-center displacements. The estimated ferroelectric polarization, obtained using the atomic positions deduced from Rietveld refinement of corresponding synchrotron x-ray diffraction (XRD) data, is found to be in excellent agreement with the FE polarization values obtained from PUND experiments. Once synthesized, the obtained room-temperature FE $Pna2_1$ structure is stable, except against further heating under ambient pressures beyond $\approx$450 K, where it converts irreversibly to the centrosymmetric $Pbnm$ phase (verified using dielectric, calorimetric, and synchrotron XRD investigations). Consistent with the previous literature, solid-state synthesized (SS) $DyCrO_3$ and $LaCrO_3$ are found to be paraelectrics at room temperature. SPS synthesized $LaCrO_3$, which is FE at room temperature, undergoes magnetic ordering at 290 K, thus coming very close to becoming the first room-temperature multiferroic material in this promising class of $RCrO_3$ compounds.

II. METHODOLOGY

SS $DyCrO_3$ (SS-DCO) and SS $LaCrO_3$ (SS-LCO) were prepared using standard solid-state synthesis [27,35]. For this, stoichiometric mixtures of Dy_2O_3, La_2O_3, and Cr_2O_3 were well ground and then calcined in two steps in air, first at 1300 °C and then at 1400 °C for 24 hours. Some parts of SS-DCO and SS-LCO, thus prepared, were subjected to spark-plasma sintering (SPS) at 1300 °C for 15 minutes under 60 MPa pressure to obtain SPS-DCO and SPS-LCO. Room-temperature synchrotron powder x-ray diffraction (XRD) using a monochromatic x-ray beam of $\lambda = 0.723$ Å for DCO (SS-DCO, SPS-DCO, and SPS-DCO-ANN) and 0.721 Å for LCO (SS-LCO, SPS-LCO, and SPS-LCO-ANN) were carried out for structural phase characterizations and Rietveld refinements of powder diffraction data were performed using FULLPROF software. The scanning electron microscopy (SEM) images collected in a secondary electron mode for SS-DCO and SPS-DCO samples confirm the polycrystalline nature of the prepared samples and also clearly point out the increase in density in SPS-DCO compared to SS-DCO, as shown in Fig. S11 of the Supplemental Material [36]. Micro Raman measurements were performed using a 514 nm laser at room temperature. The ferroelectric-polarization–electric-field (P-E) loop and positive up–negative down (PUND) measurements were also conducted using a radiant P-E loop tracer [37–39]. Piezoresponse force microscopy (PFM) measurements were performed with 10 V, 150 Hz ac bias in contact mode to visualize polar domains. The dc magnetic and dielectric permittivity measurements were carried out with the help of a superconducting quantum interference device (SQUID) magnetometer and a LCR meter, respectively. Differential scanning calorimetric (DSC) measurements were also performed both in heating and cooling cycles to investigate the phase-transition temperature.

III. RESULTS AND DISCUSSIONS

Owing to similarities and to maintain brevity and focus, we will primarily discuss the methodologies and results involving $DyCrO_3$ in this manuscript and discuss the important results on $LaCrO_3$ towards the latter part of the manuscript. As seen through the synchrotron XRD data in Fig. 2(a) and room-temperature Raman data in Fig. 2(b), both SS-DCO and SPS-DCO are single phase and appear to be structurally similar [40–42]. SPS-DCO, however, exhibits distinct peak broadenings in comparison to SS-DCO, both in the XRD and Raman data (mainly in modes related to Dy^{3+} ions and surrounding oxygen ions [41,42]), the origin of which will be discussed in further details later in the manuscript. Interestingly, we find a finite, though somewhat lossy, electric-polarization (P) vs electric-field (E) loop at room temperature in SPS-DCO [shown in the inset of Fig. 3(a)]. In order to verify whether SPS-DCO is FE at room temperature, we adopted the PUND FE characterization technique since it is a well-established and sensitive tool to extract intrinsic FE from other extrinsic contributions [26,27,38,39,43–45]. Remarkably, the room-temperature PUND results, as shown in Figs. 3(a)–3(c), confirm the existence of finite, switchable intrinsic FE remanent polarization ($dP_r = 0.31 \pm 0.01\ \mu C/cm^2$) in SPS-DCO. Also, as seen in Figs. 3(d)–3(f), different amplitude and phase

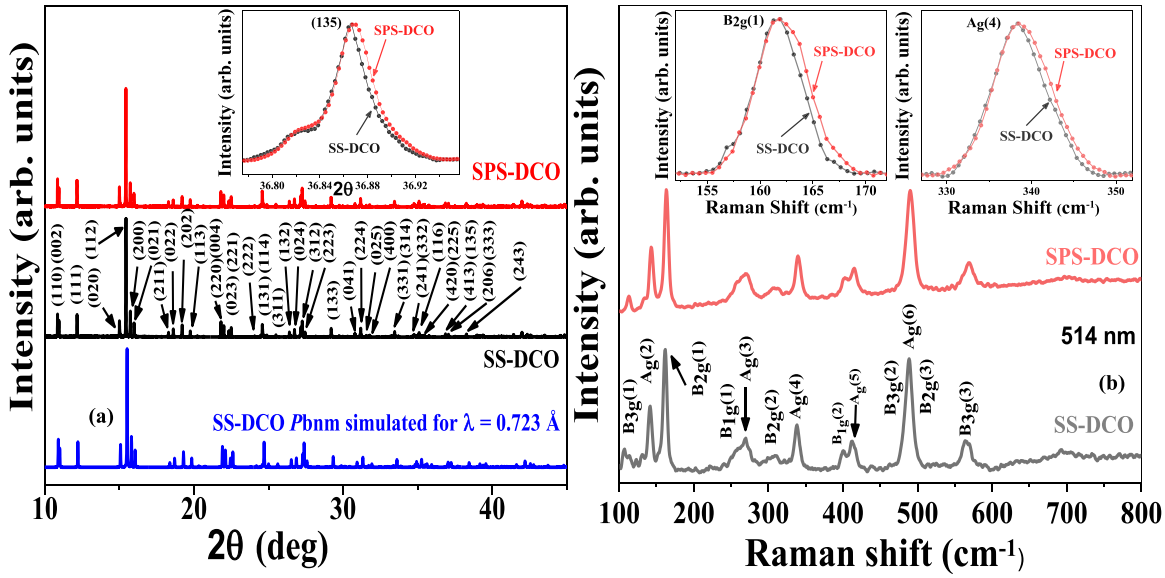

FIG. 2. (a) Room-temperature synchrotron XRD spectra of SPS-DCO and SS-DCO. (b) Room-temperature Raman spectra of SPS-DCO and SS-DCO. The corresponding insets show comparisons of a few of the representative peaks, which suggest that although structurally similar and single phase, SPS-DCO does exhibit distinct peak broadenings as compared to SS-DCO.

contrast regions (corresponding to different ferroelectric domains) are identifiable in the piezoresponse force microscopy (PFM) data on SPS-DCO at room temperature. While, due to the lossy nature of SS-DCO, reliable PUND measurements could not be carried out, PFM data on SS-DCO clearly show the absence of any piezoresponse, as seen in Figs. 3(g)–3(i), elucidating the room-temperature paraelectric state in SS-DCO in contrast to the FE SPS-DCO.

In order to investigate any role of magnetism to the observed room-temperature FE in SPS-DCO, temperature- (T) and magnetic-field- (H) dependent magnetization (M) measurements were carried out. As seen through the corresponding M-T and inverse magnetic-susceptibility $\chi^{-1} - T$ data of SPS-DCO in Fig. 4 and its upper inset, SPS-DCO undergoes a paramagnetic (PM) to antiferromagnetic (AFM) transition at ≈145 K. This is also consistent with a linear room-temperature M-H loop (without trace of any hysteresis) of SPS-DCO, as seen in the lower inset of Fig. 4. Importantly, all the above magnetic properties of SPS-DCO, including the PM to AFM transition temperature, are nearly identical to that of SS-DCO (as seen in Fig. S3 and its insets in the Supplemental Material [36]) [42,46,47]. Thus, any role of magnetism to the observed room-temperature FE in SPS-DCO can be clearly ruled out.

A small increment in the relative dielectric permittivity (ϵ'_r) values of polycrystalline SS-DCO below ≈50 K [illustrated by the shaded region in Fig. 5(a)] seems consistent with a low-temperature increase in ϵ'_r seen in single-crystalline $DyCrO_3$ (albeit at slightly higher temperatures) and that is reported to arise as a consequence of the quantum-paraelectric nature of $DyCrO_3$ [28]. For single-crystalline $DyCrO_3$, a small increase (≈0.13) in ϵ'_r is found to arise only along the c axis below 150 K (along other perpendicular two-axes, ϵ'_r decreases with lowering of temperature). Understandably, due to the averaging effect in polycrystalline samples, the corresponding rise in ϵ'_r will become weaker and observable only at further lower temperature. Since SS-DCO do not exhibit any other transition around ≈50 K, the weak rise in ϵ'_r below ≈50 K is understood to arise due to its reported quantum-paraelectric state. At further lower temperatures of ≈20 K, the spin-reorientation transition of Dy^{3+} spins in $DyCrO_3$ leads to a further increase [seen in Fig. 5(a)] in ϵ'_r values of $DyCrO_3$ [48]. Interestingly, while the rise in ϵ'_r values is clearly observable below the spin-reorientation transition in the case of both SPS-DCO and SS-DCO, any rise in ϵ'_r values is not observed for SPS-DCO below ≈50 K, likely suggesting the melting of the corresponding quantum-paraelectric state in SPS-DCO. Further, a clear peak in T-dependent ϵ'_r and dielectric loss data (collected during heating run under ambient pressure), which does not disperse with varying electric-field frequencies, as seen in Figs. 5(b), clearly suggests that SPS-DCO undergoes a FE to paraelectric (presumably) phase transition at ≈440 K. The transition at ≈440 K in SPS-DCO also becomes clearly evident in the corresponding DSC data collected on SPS-DCO during the heating run, as seen in Fig. 5(d). Consistent with the room-temperature paraelectric state of SS-DCO, such a high-temperature dispersionless phase transition is not observable in the corresponding $\epsilon'_r - T$ data (which instead exhibits strong Maxwell-Wagner dielectric relaxation, marked as B in Fig. 5(c) [49–51]; the dielectric relaxation A at lower temperatures, which is similarly found in the case of SPS-DCO, is currently being investigated in further detail). Similarly, the DSC data of SS-DCO, collected in the heating run, do not exhibit a signature of any high-temperature phase transition, as seen in the inset to Fig. 5(d). Importantly, the observed FE in SPS-DCO is found to be reproducible and stable at room temperature over a gap of many months (the maximum that we have checked for is after a gap of 12 months), as shown in Fig. S4 of the Supplemental Material [36]. As the contributions from grain boundary and porosity present in SS-DCO are drastically reduced in SPS-DCO (as evident from the

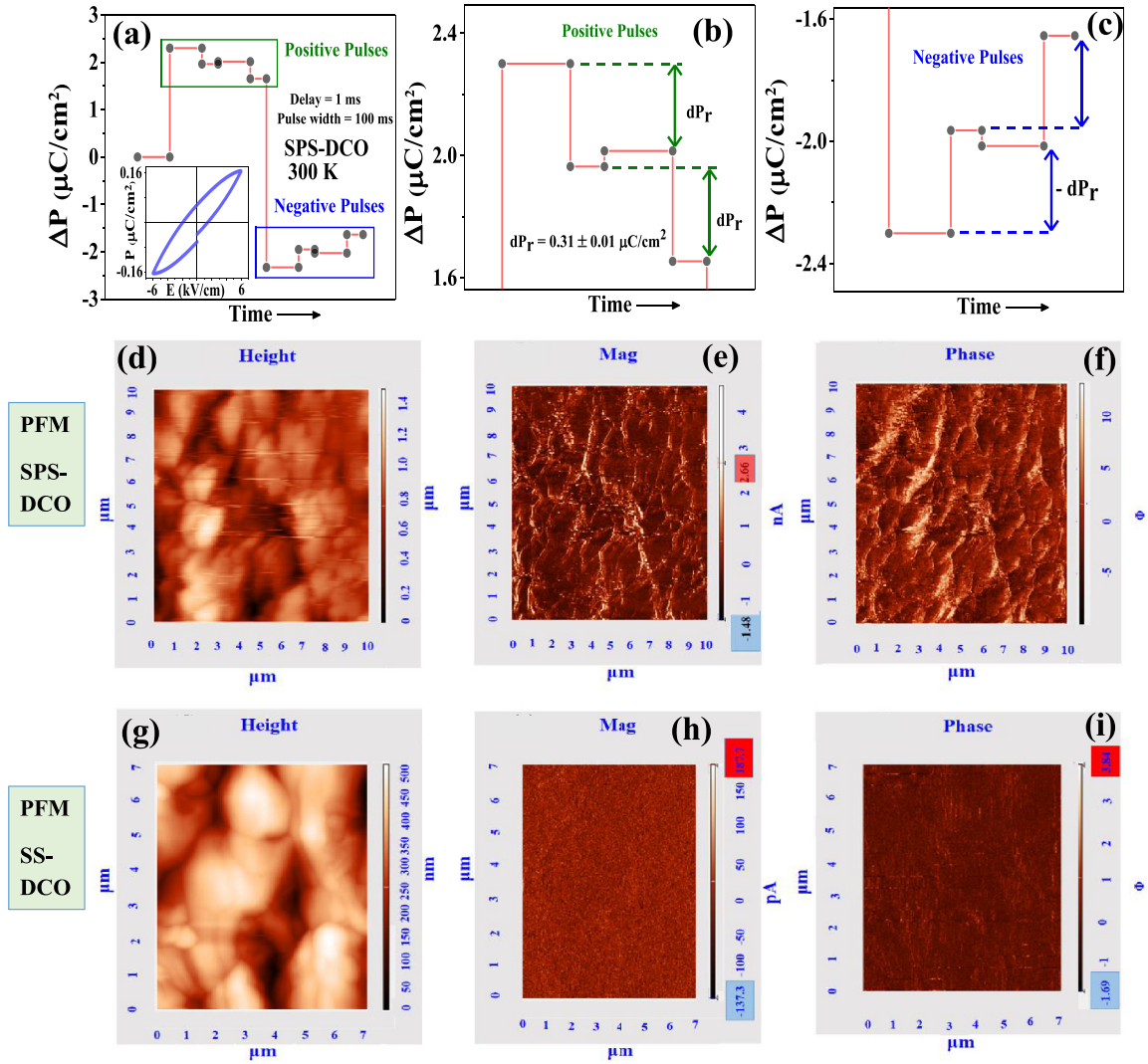

FIG. 3. (a) Room-temperature PUND data at 6 kV/cm applied electric field on SPS-DCO (the inset shows the room-temperature *P-E* loop of SPS-DCO collected at a frequency of 50 Hz). (b),(c) Enlarged views of the switchable electric polarization responses under positive and negative electric pulses of PUND data. Room-temperature (d) topographical AFM, (e) amplitude contrast, and (f) phase contrast PFM images (color contrast present in the phase image corresponds to the signature of piezoelectricity in the compound) of SPS-DCO. (g)–(i) Topographical AFM and the absence of amplitude and phase contrast in the PFM images of SS-DCO.

corresponding SEM images as shown in Figs. S11(a) and S11(b) of the Supplemental Material [36] and from Cole-Cole plots, shown in Figs. S12(a) and S12(b) of the Supplemental Material [36]), and as the room-temperature ferroelectric phase has been obtained in SPS-DCO (with DC resistivity $\sim 2 \times 10^9$ Ω cm) in contrast to the room-temperature paraelectric phase in SS-DCO (with DC resistivity $\sim 5 \times 10^5$ Ω cm), any contribution of any frozen dipole moments at the grain-boundary region can be clearly ruled out [52–54].

To investigate whether the obtained room-temperature FE in SPS-DCO is a thermodynamically stabilized or kinetically stabilized phase, T-dependent ϵ'_r in subsequent heating cycles and DSC measurements in subsequent cooling and heating cycles were performed under ambient-pressure condition. Interestingly, the peak in ϵ'_r in subsequent heating and the corresponding peak in the DSC cooling at ≈440 K are absent, as seen in Fig. S1 of the Supplemental Material [36]. To further verify this, SPS-DCO had been further annealed at 1300 °C in air under ambient -pressure condition and slowly cooled to room temperature to form SPS-DCO-ANN. Consistent with the paraelectric state of SPS-DCO-ANN at room temperature, the corresponding PFM data (shown in Figs. S2(d)–S2(f) in the Supplemental Material [36]) do not show any phase and amplitude contrast. These measurements, thus, clearly elucidate that room-temperature FE in SPS-DCO is a kinetically arrested phase, which is unstable against heating of the sample beyond ≈440 K.

In order to understand the structural phase responsible for room-temperature FE in SPS-DCO, we refer to our earlier first-principles calculations on the relative energy stability among the various possible structural space groups in the $RCrO_3$ compounds [27]. Results from our first-principles calculation, which are also consistent with other similar investigations [25], suggest that two structural space groups, i.e., centrosymmetric *Pbnm* and non-centrosymmetric $Pna2_1$, are energetically more favorable (the energy difference

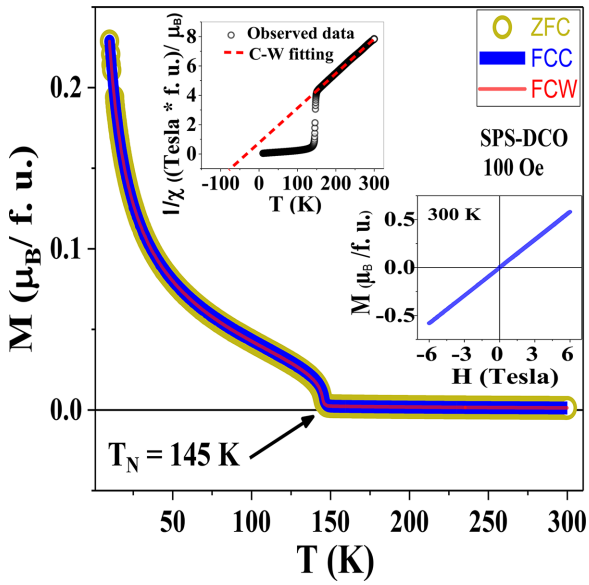

FIG. 4. Temperature (T) dependence of magnetization (M) of SPS-DCO collected in zero-field-cooled heating (ZFC), field-cooled cooling (FCC), and field-cooled warming (FCW) modes with applied magnetic field (H) of 100 Oe (the upper inset shows $\chi^{-1} - T$ data, which clearly highlight the antiferromagnetic ordering, and the lower inset illustrates the linear dependence of M on H, highlighting the paramagnetic state at room temperature).

between these two structures is within our calculation error limit) in the case of many of the $R\mathrm{CrO_3}$ compounds. Consistent with the above, the paraelectric to ferroelectric phase transition in $R\mathrm{CrO_3}$ materials has also been ascribed

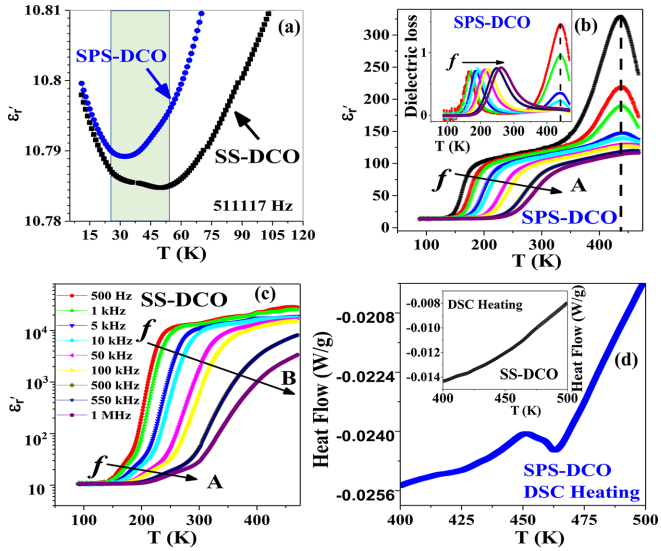

FIG. 5. (a) Comparison of relative dielectric permittivity (ϵ_r') of SPS-DCO and SS-DCO collected at 511117 Hz. Temperature (T) dependencies of relative dielectric permittivity (ϵ_r') at various electric-field frequencies of (b) SPS-DCO and (c) SS-DCO. The inset to (b) shows the corresponding dielectric loss data of SPS-DCO. (d) T-dependent DSC heating data of SPS-DCO highlighting a similar higher-temperature transition (the inset shows the DSC data of SS-DCO, taken in the heating cycle, that exhibits the absence of any corresponding transition).

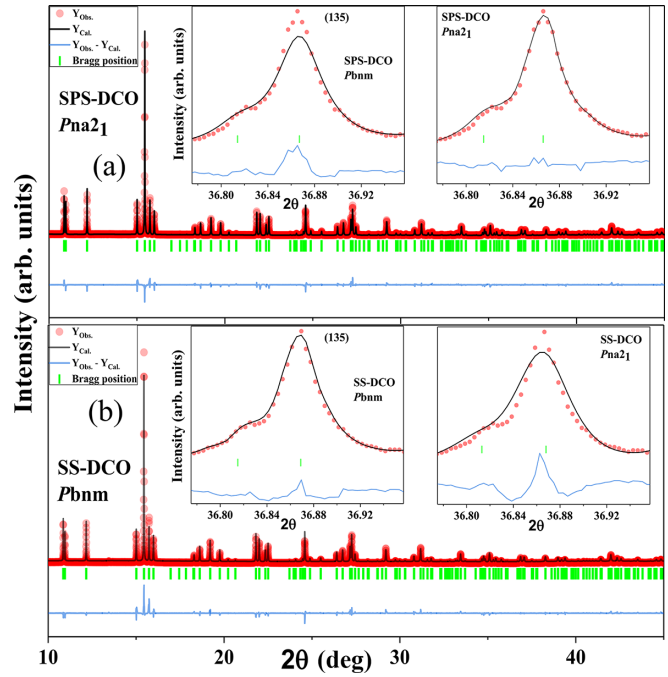

FIG. 6. (a) The Rietveld refinement of room-temperature synchrotron XRD spectra of SPS-DCO considering the $Pna2_1$ space group. The left and right insets show the (135) peak of SPS-DCO, refined with the $Pbnm$ ($R_p = 10.4$, $R_{wp} = 13.6$, $\chi^2 = 4.08$) and $Pna2_1$ ($R_p = 9.26$, $R_{wp} = 13.0$, $\chi^2 = 3.73$) space groups, respectively. (b) The Rietveld refinement of room-temperature synchrotron XRD spectra of SS-DCO with the $Pbnm$ space group. The left and right insets show the (135) peak of SS-DCO, refined with the $Pbnm$ ($R_p = 10.5$, $R_{wp} = 14.5$, $\chi^2 = 3.86$) and $Pna2_1$ ($R_p = 11.1$, $R_{wp} = 15.3$, $\chi^2 = 4.30$) space groups, respectively.

to a phase transition between the $Pbnm$ to the $Pna2_1$ structures, respectively [25,55,56]. Accordingly, we have refined the room-temperature synchrotron XRD spectra of SS-DCO and SPS-DCO by adapting both the $Pbnm$ and the $Pna2_1$ space groups (refined lattice parameters are shown in Table I; see Supplemental Material [36]). Interestingly, while the room-temperature XRD spectrum of SPS-DCO can be better fitted using the noncentrosymmetric $Pna2_1$ space group, the same for SS-DCO can be better accounted for by adapting the centrosymmetric $Pbnm$ space group, as seen in Fig. 6. In addition, the structure of SPS-DCO-ANN, as determined from room-temperature synchrotron XRD data, is found to be better described with centrosymmetric $Pbnm$, consistent with its room-temperature paraelectric state (shown in Figs. S2(a)–S2(c) of the Supplemental Material [36]). Using the refined structural parameters of the $Pna2_1$ space group for SPS-DCO, the ionic contribution to the ferroelectric polarization was calculated using the formula reported in Refs. [27,56]. Significantly, the calculated ionic contribution to the FE polarization is $\approx 0.1117 \pm 0.0001\ \mu C/cm^2$, which agrees very well with the remanent FE polarization value (i.e., $P = 0.155 \pm 0.01\ \mu C/cm^2$, where $P = \frac{1}{2}\, dP_r$) obtained in room-temperature PUND experiments on SPS-DCO.

Further, we also report intrinsic room-temperature ferroelectricity in SPS-LCO [the results of room-temperature P-E and PUND measurements are shown in Figs. 7(a)–7(c)],

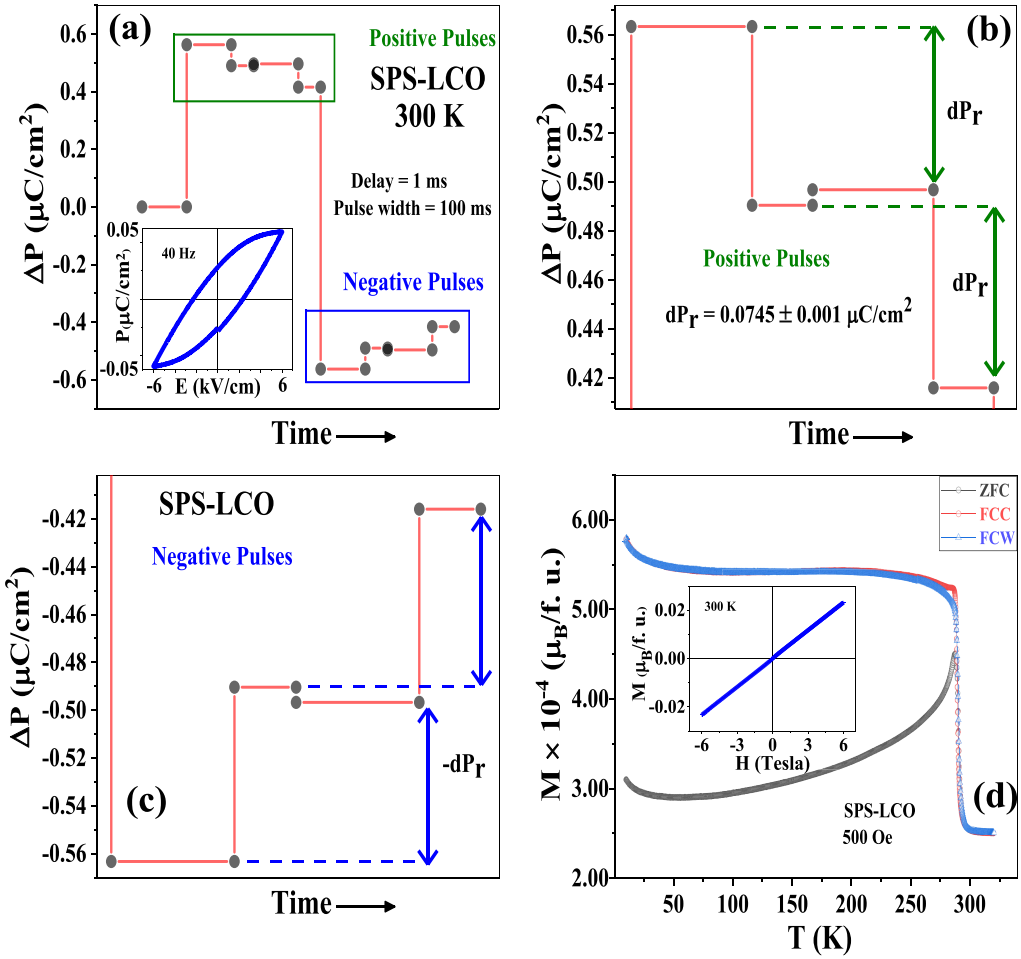

FIG. 7. (a) Room-temperature PUND data of SPS-LCO collected with 6 kV/cm applied electric field (the inset shows the room-temperature *P-E* loop of SPS-LCO recorded at a frequency of 40 Hz). (b),(c) Enlarged views of the switchable electric-polarization responses under positive and negative electric pulses of PUND data. (d) ZFC, FCC, and FCW *M-T* data of SPS-LCO indicate an antiferromagnetic transition at around 290 K. Linear *M-H* data in the corresponding inset indicate a paramagnetic state of SPS-LCO at room temperature.

whereas SS-LCO remains paraelectric (supporting data are shown in Fig. S6(d) and Fig. S9(b) of the Supplemental Material [36]), as reported earlier. Consistent with the above, SPS-LCO and SS-LCO are found to crystallize in the non-centrosymmetric $Pna2_1$ and centrosymmetric *Pbnm* phases at room temperature, respectively (the corresponding synchrotron XRD and refinement results are shown in Fig. S8, Fig. S9, and Table II of the Supplemental Material [36]). Interestingly, both SPS-LCO and SS-LCO undergo AFM ordering just below room temperature, at ≈290 K (the *M-T* data of SPS-LCO are shown in Fig. 7(d) and the corresponding data of SS-LCO are shown in Fig. S5 of the Supplemental Material [36]) [30–32,57]. The room-temperature ferroelectricity in SPS-LCO, while reproducible and stable at room temperature, undergoes a similar irreversible FE to paraelectric phase transition (the corresponding dispersionless transition in ϵ'_r-*T* and DSC data, collected during the heating runs, are included in Figs. S6(a)–S6(c) of the Supplemental Material [36]) at high temperatures, similar to SPS-DCO (Fig. S7 of the Supplemental Material [36]). A similarly annealed SPS-LCO, SPS-LCO-ANN (annealed under similar conditions as SPS-DCO-ANN) is found to crystallize in the centrosymmetric *Pbnm* phase (corresponding synchrotron XRD data and refinement results are shown in Fig. S10 of the Supplemental Material [36]), establishing the kinetic origin of ferroelectricity in SPS-LCO. SPS-LCO, however, exhibits a lower FE polarization as compared to SPS-DCO at room temperature, likely because the ionic radius of La^{3+} ions is much larger than Dy^{3+}, which causes a smaller magnitude of off-center displacement of the La^{3+} ion in SPS-LCO compared to the Dy^{3+} ion in SPS-DCO. Also, the calculated ionic contribution to the ferroelectric polarization, using the refined atomic positions (from synchrotron XRD refinement results) of SPS-LCO, is ≈0.01908 ± 0.0001 μC/cm², which is in good agreement with the experimentally determined remanent FE polarization value (≈0.0373 ± 0.001 μC/cm²) of SPS-LCO. Significantly, SPS-LCO becomes multiferroic below ≈290 K, which is the highest in this $RCrO_3$ family and is very close to becoming a room-temperature multiferroic material.

IV. CONCLUSIONS

In summary, while $DyCrO_3$ and $LaCrO_3$ are known to be quantum-paraelectric and a paraelectric materials,

respectively, we successfully engineer room-temperature ferroelectricity in both of these compounds, when synthesized using a modified protocol that involves spark-plasma sintering (SPS) at high temperatures. Although, theoretically, ferroelectric (FE) instability over antiferrodistortive (AFD) nonpolar modes has been predicted, this is an experimental realization of FE in either of these compounds. In contrast, the solid-state synthesized (SS) $DyCrO_3$ and $LaCrO_3$ are found to remain paraelectrics, following earlier reports. Significantly, while the magnetic properties remain similar between the SPS and SS synthesized compounds and they undergo antiferromagnetic ordering at temperatures lower than room temperature, the room-temperature FE in both of the SPS synthesized compounds is found to be of structural origin, arising from off-centering displacements of rare-earth R and Cr ions. The room-temperature FE phase arises from a kinetically arrest process during SPS, which likely favors the FE instability modes over the AFD modes in this emerging family of $RCrO_3$ multiferroic compounds.

ACKNOWLEDGMENTS

S.M. would like to acknowledge the financial support from MoE, India. D.C. acknowledges STARS, MoE, India (Grant No. MoE-STARS/STARS-1/238) for financial support. S.M. and D.C. would like to acknowledge the use of the Raman spectroscopy and SPS central facilities at IIT Kharagpur. D.C. would like to acknowledge insightful discussions with Prof. D. D. Sarma.

[1] H. Schmid, Ferroelectrics **162**, 317 (1994).
[2] D. Khomskii, Physics **2**, 20 (2009).
[3] T. Kimura, T. Goto, H. Shintani, K. Ishizaka, and Y Tokura, Nature (London) **426**, 55 (2003).
[4] W. Eerenstein, N. D. Mathur, and J. F. Scott, Nature (London) **442**, 759 (2006).
[5] J. F. Scott, Nat. Mater. **6**, 256 (2007).
[6] N. A. Spaldin, S.-W. Cheong, and R Ramesh, Phys. Today **63**(10), 38 (2010).
[7] M. M. Vopson, Crit. Rev. Solid State Mater. Sci. **40**, 223 (2015).
[8] R. E. Cohen and H. Krakauer, Phys. Rev. B **42**, 6416 (1990).
[9] R. E. Cohen, Nature (London) **358**, 136 (1992).
[10] Ph. Ghosez, E. Cockayne, U. V. Waghmare, and K. M. Rabe, Phys. Rev. B **60**, 836 (1999).
[11] S. Bhattacharjee, E. Bousquet, and P Ghosez, Phys. Rev. Lett. **102**, 117602 (2009).
[12] W. Zhong and D Vanderbilt, Phys. Rev. Lett. **74**, 2587 (1995).
[13] C.-J. Eklund, C. J. Fennie, and K. M. Rabe, Phys. Rev. B **79**, 220101(R) (2009).
[14] R. Xu, J. Huang, E. S. Barnard, S. S. Hong, P. Singh, E. K. Wong, T. Jansen, V Harbola, J. Xiao, B. Y. Wang, S. Crossley, D. Lu, S. Liu, and H. Y. Hwang, Nat. Commun. **11**, 3141 (2020).
[15] M. D. Biegalski, L. Qiao, Y. Gu, A. Mehta, Q. He, Y. Takamura, A. Borisevich, and L.-Q. Chen, Appl. Phys. Lett. **106**, 162904 (2015).
[16] A. Marthinsen, C. Faber, U. Aschauer, N. A. Spaldin, and S. M. Selbach, MRS Commun. **6**, 182 (2016).
[17] J. Hong and D. Vanderbilt, Phys. Rev. B **87**, 064104 (2013).
[18] C. Ederer, T. Harris, and R. Kováčik, Phys. Rev. B **83**, 054110 (2011).
[19] J. M. Rondinelli, A. S. Eidelson, and N. A. Spaldin, Phys. Rev. B **79**, 205119 (2009).
[20] J. H. Lee and K. M. Rabe, Phys. Rev. Lett. **104**, 207204 (2010).
[21] H. Sakai, J. Fujioka, T. Fukuda, D Okuyama, D. Hashizume, F. Kagawa, H Nakao, Y. Murakami, T. Arima, A. Q. R. Baron, Y. Taguchi, and Y. Tokura, Phys. Rev. Lett. **107**, 137601 (2011).
[22] H. An, Y.-G. Choi, Y.-R. Jo, H. J. Hong, J.-K. Kim, O. Kwon, S. Kim, M. Son, J. Yang, J.-C. Park, H. Choi, J. Lee, J. Song, M.-H Ham, S. Ryu, Y. Kim, C. W. Bark, K.-T. Ko, B.-J. Kim, and S. Lee, NPG Asia Mater. **13**, 69 (2021).
[23] T. Günter, E. Bousquet, A. David, P. Boullay, P. Ghosez, W. Prellier, and M. Fiebig, Phys. Rev. B **85**, 214120 (2012).
[24] C. R. Serrao, A. K. Kundu, S. B. Krupanidhi, U. V. Waghmare, and C. N. R. Rao, Phys. Rev. B **72**, 220101(R) (2005).
[25] S. Mahana, B. Rakshit, R. Basu, S. Dhara, B. Joseph, U. Manju, S. D. Mahanti, and D. Topwal, Phys. Rev. B **96**, 104106 (2017).
[26] B. Rajeswaran, D. I. Khomskii, A. K. Zvezdin, C. N. R. Rao, and A. Sundaresan, Phys. Rev. B **86**, 214409 (2012).
[27] S. Mishra, Keerthana, K Rudrapal, A. Rahaman, P. Pal, A. Sagdeo, R. Mishra, D. Topwal, A. R. Chaudhuri, V. Adyam, and D. Choudhury, Phys. Rev. B **104**, L180101 (2021).
[28] L. H. Yin, T. F. Shi, R. R. Zhang, C. B. Park, K. H. Kim, J. Yang, P. Tong, W. H. Song, J. M. Dai, X. B. Zhu, W. S. Yan, and Y. P. Sun, Phys. Rev. B **98**, 054301 (2018).
[29] K. A. Müller and H. Burkard, Phys. Rev. B **19**, 109 (1979).
[30] J. R. Sahu, C. R. Serrao, N. Ray, U. V. Waghmare, and C. N. R. Rao, J. Mater. Chem. **17**, 42 (2007).
[31] K. Yoshii, N. Ikeda, Y. Shimojo, and Y. Ishii, Mater. Chem. Phys. **190**, 96 (2017).
[32] H-Y. Guo, J. I. L Chen, and Z-G Ye, J. Mater. Res. **22**, 2081 (2007).
[33] N. Ray, and U. V. Waghmare, Phys. Rev. B **77**, 134112 (2008).
[34] J. Hong, A. Stroppa, J. Íñiguez, S. Picozzi, and D. Vanderbilt, Phys. Rev. B **85**, 054417 (2012).
[35] S. Mahana, U. Manju, and D. Topwal, J. Phys. D: Appl. Phys. **51**, 305002 (2018).
[36] See Supplemental Material at http://link.aps.org/supplemental/10.1103/PhysRevB.107.214104 for additional dielectric, PUND, magnetization, DSC, structural data and SEM images.
[37] J. T. Evans, Proc. IEEE ISAF 1 (2011).
[38] A. R. Chaudhuri and S. B. Krupanidhi, Solid State Commun. **150**, 660 (2010).
[39] P. Pal, K. Rudrapal, S. Mahana, S. Yadav, T. Paramanik, S. Mishra, K. Singh, G. Sheet, D. Topwal, A. R. Chaudhuri, and D. Choudhury, Phys. Rev. B **101**, 064409 (2020).
[40] J. P. Gonjal, R. Schmidt, J.-J. Romero, D. Ávila, U. Amador, and E. Morán, Inorg. Chem. **52**, 313 (2013).
[41] M. C. Weber, J. Kreisel, P. A. Thomas, M. Newton, K. Sardar, and R. I. Walton, Phys. Rev. B **85**, 054303 (2012).
[42] A. McDannald, L. Kuna, and M. Jain, J. Appl. Phys. **114**, 113904 (2013).
[43] R. Saha, A. Sundaresan, and C. N. R Rao, Mater. Horiz. **1**, 20 (2014).

[44] Y. S. Chai, Y. S. Oh, L. J. Wang, N. Manivannan, S. M. Feng, Y. S. Yang, L. Q. Yan, C. Q. Jin, and K. H. Kim, Phys. Rev. B **85**, 184406 (2012).
[45] S. M. Feng, Y. S. Chai, J. L. Zhu, N. Manivannan, Y. S. Oh, L. J. Wang, Y. S. Yang, C. Q. Jin, and K. H. Kim, New J. Phys. **12**, 073006 (2010).
[46] E. T. Sibanda, A. R. E. Prinsloo, C. J. Sheppard, and P. Mohanty, AIP Adv. **12**, 035342 (2022).
[47] A. McDannald, L. Kuna, M. S. Seehra, and M. Jain, Phys. Rev. B **91**, 224415 (2015).
[48] L. H. Yin, J. Yang, P. Tong, X. Luo, C. B. Park, K. W. Shin, W. H. Song, J. M. Dai, K. H. Kim, X. B. Zhua, and Y. P. Sun, J. Mater. Chem. C **4**, 11198 (2016).
[49] A. R. von Hippel, *Dielectrics and Waves* (MIT Press, Cambridge, MA, 1966).
[50] D. Choudhury, P. Mandal, R. Mathieu, A. Hazarika, S. Rajan, A. Sundaresan, U. V. Waghmare, R. Knut, O. Karis, P. Nordblad, and D. D. Sarma, Phys. Rev. Lett. **108**, 127201 (2012).
[51] V. K. Anusree, P. N. Lekshmi, S. G. Bhat, A. A. Wagh, G. Das, and P. N Santhosh, J. Appl. Phys. **127**, 194105 (2020).
[52] V. Buscaglia, M. T. Buscaglia, M. Viviani, L. Mitoseriu, P. Nanni, V. Trefiletti, P. Piaggio, I. Gregora, T. Ostapchuk, J. Pokorný, and J. Petzelt, J. Eur. Ceram. Soc. **26**, 2889 (2006).
[53] J. Petzelt, T. Ostapchuk, I. Gregora, I. Rychetský, S. Hoffmann-Eifert, A. V. Pronin, Y. Yuzyuk, B. P. Gorshunov, S. Kamba, V. Bovtun, J. Pokorný, M. Savinov, V. Porokhonskyy, D. Rafaja, P. Vaněk, A. Almeida, M. R. Chaves, A. A. Volkov, M. Dressel, and R. Waser, Phys. Rev. B **64**, 184111 (2001).
[54] J. Petzelt, T. Ostapchuk, I. Gregora, P. Kuzel, J. Liu, and Z. Shen, J. Phys.: Condens. Matter **19**, 196222 (2007).
[55] A. Ghosh, A. Pal, K. Dey, S. Majumdar, and S. Giri, J. Mater. Chem. C **3**, 4162 (2015).
[56] A. Ghosh, K. Dey, M. Chakraborty, S. Majumdar, and S. Giri, Europhys. Lett. **107**, 47012 (2014).
[57] J.-S. Zhou, J. A. Alonso, A. Muoñz, M. T. Fernández-Díaz, and J. B. Goodenough, Phys. Rev. Lett. **106**, 057201 (2011).